

# Motif Channel Opened in a White-Box: Stereo Matching via Motif Correlation Graph

Ziyang Chen<sup>✉</sup>, Student Member, IEEE, Yongjun Zhang<sup>\*✉</sup>, Member, IEEE, Wenting Li<sup>✉</sup>,  
Bingshu Wang<sup>✉</sup>, Yong Zhao<sup>✉</sup>, Member, IEEE, C. L. Philip Chen<sup>✉</sup>, Life Fellow, IEEE

**Abstract**—Real-world applications of stereo matching, such as autonomous driving, place stringent demands on both safety and accuracy. However, learning-based stereo matching methods inherently suffer from the loss of geometric structures in certain feature channels, creating a bottleneck in achieving precise detail matching. Additionally, these methods lack interpretability due to the black-box nature of deep learning. In this paper, we propose MoCha-V2, a novel learning-based paradigm for stereo matching. MoCha-V2 introduces the Motif Correlation Graph (MCG) to capture recurring textures, which are referred to as “motifs” within feature channels. These motifs reconstruct geometric structures and are learned in a more interpretable way. Subsequently, we integrate features from multiple frequency domains through wavelet inverse transformation. The resulting motif features are utilized to restore geometric structures in the stereo matching process. Experimental results demonstrate the effectiveness of MoCha-V2. MoCha-V2 achieved 1st place on the Middlebury benchmark at the time of its release. Code is available at here.

**Index Terms**—Stereo Matching, Motif, White Box, Deep Learning.

## 1 INTRODUCTION

**S**TEREO matching is a key component in computer vision applications, particularly in the fields of autonomous driving [1], [2], [3], [4], medical care [5], [6], [7], 3D reconstruction [8], [9], [10], and remote sensing [11], [12], [13]. Creating a pixel-level disparity map is the main goal of binocular stereo matching [14]. This map can be used to calculate the depth of pixels in an image. The edge performance of the disparity map is particularly important for pixel-level rendering technologies such as virtual reality and augmented reality, where the exact match between scene model and image mapping is critical. This emphasises the importance of keeping the edges of the disparity map and the original RGB image precisely aligned.

Traditional stereo matching schemes include global [16], semi-global [17] and local [18] approaches. All of these manual methods [19], [20], [21], [22] are difficult to adapt to the changing and complex scenarios of the real world [14], [23]. With the development of deep learning [24], learning-based methods have exhibited great potential in this field. Stereo convolutional neural networks (CNNs) [25] typically consist of five steps: feature extraction, cost volume

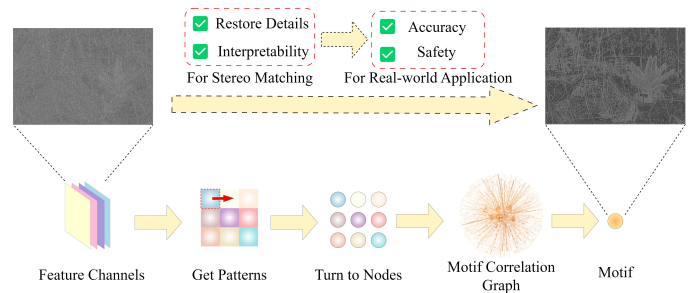


Fig. 1. In the deep learning process, feature channels are extended to higher dimensions. During this process, the geometric details learned in individual feature channels are inevitably lost. We propose that these details can be recovered by identifying recurrent geometric structures across the channels. MoCha-V2 constructs a directed graph, i.e., motif correlation graph (MCG), to capture frequent patterns in feature channels. Specifically, MCG leverages node weights to detect recurring geometric structures within the channels. MCG establishes a robust and stable framework for identifying repetitive geometric structures. Due to its interpretability, MoCha-V2 also demonstrates significant potential for safety-critical real-world applications.

construction, cost aggregation, disparity computation, and disparity refinement [26]. Cost volume gives preliminary similarity estimates for left image pixels and perhaps comparable right image pixels. The accuracy and computational complexity of the final result depend heavily on a clear and informative cost volume representation from this phase. A number of studies have been carried out to develop more accurate matching costs. A common approach is to construct a 4D cost volume [14], [27], [28]. Specifically, 4D cost volume connects the left feature map with its corresponding right feature map and records the disparity at this point to form a cost volume. This process constructs a space with dimensions of  $height \times width \times disparity \times feature\ values$ , which serves as the cost volume. To reduce computational costs, RAFT-Stereo [29] designed a 3D correlation pyramid

- Ziyang Chen and Yongjun Zhang are with the College of Computer Science, the State Key Laboratory of Public Big Data, Guizhou University, Guiyang 550025, China.  
E-mail: ziyangchen2000@gmail.com, zyj6667@126.com
- Wenting Li is with the School of Information Engineering, Guizhou University of Commerce, Guiyang 550021, China.  
E-mail: 201520274@gzcc.edu.cn
- Bingshu Wang is with the School of Software, Northwestern Polytechnical University, Xi'an, 710129, China.  
E-mail: wangbingshu@nwpu.edu.cn
- Yong Zhao is with the Key Laboratory of Integrated Microsystems, Shenzhen Graduate School, Peking University, Shenzhen 518055, China.  
E-mail: zhaoyong@pku.edu.cn
- C. L. Philip Chen is with the School of Computer Science and Engineering, South China University of Technology, Guangzhou 510641, China.  
E-mail: philip.chen@ieee.org

\* Corresponding author: Yongjun Zhang.

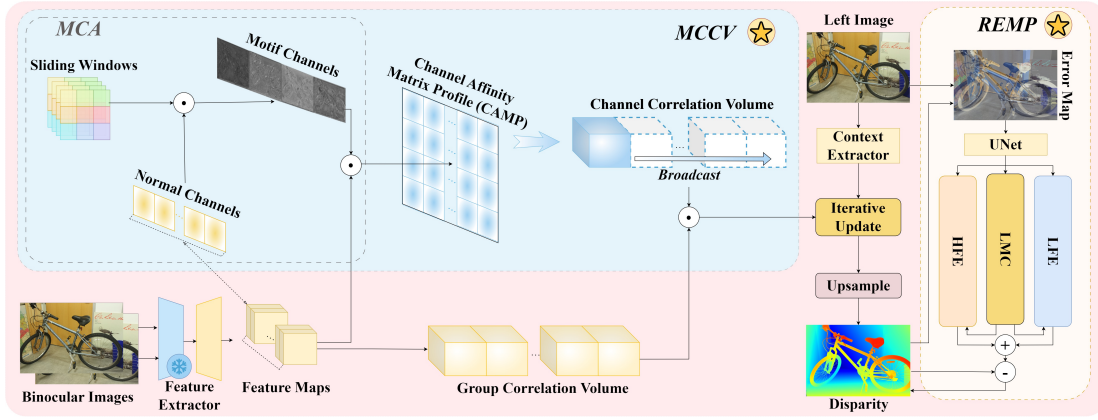


Fig. 2. Pipeline of our previous work, MoCha-Stereo [15]. MoCha-Stereo first constructs the Motif Channel Correlation Volume (MCCV). MCCV is build by projecting the relationship between motif channels and normal channels into the basic group correlation volume. Subsequently, we employ a iterative update operator to caculate a disparity, accroding to the correlation value. Finally, the Reconstruction Error Motif Penalty (REMP) module is applied to penalize the generation of the full-resolution disparity map. In REMP, *LFE* refers to the Low-frequency Error branch, *LMC* denotes to the Latent Motif Channel branch, and *HFE* means the High-frequency Error branch.

[30]. Building on this, IGEV-Stereo [31] incorporated the concept of group-wise cost volume [32], proposing Combined Geometry Encoding Volume (CGEV). CGEV encodes the geometric relationship between the left and right views.

Another line of research posits that low-level features are the primary factors affecting detail matching. Therefore, these studies focus on optimizing the feature extraction process. SegStereo [33] improves feature learning using a semantic segmentation network [34], [35]. EdgeStereo [36] employs an edge detection network to optimize the extracted features. Similar to the Convolutional Block Attention Module (CBAM) [37] used for low-level vision tasks, Selective-Stereo [38] integrates contextual spatial attention, achieving state-of-the-art (SOTA) performance.

Although existing methods attempting to optimize the network from multiple steps, SOTA stereo matching methods still struggle to accurately match details. As illustrated in Figure 1, we believe this occurs because CNNs are essentially black-box nonlinear transformations. CNNs map images from low-dimensional to high-dimensional spaces, and this process cannot guarantee appropriate activation values for each channel. The unbalanced activation inevitably leads to the loss of edge texture information. This viewpoint can be validated through the visualization of CNNs [39], [40].

As our previous conference version, MoCha-Stereo [15] is proposed with above visions in thoughts. Inspired by “motif” [41] in time series mining, we introduce the concept of the “motif channel” [15]. In time series analysis, recurring segments of time sequences are called “motifs”. Similarly, recurrent geometric structures exist within the feature channels of images. We refer to the feature channel that encapsulates this repeated geometric information as the “motif channel”. These geometric structures help to recover missing edge information in the feature channels. As shown in Figure 2, we employ a sliding window to capture the motif channels. We then map the motif channel back to the original feature channel to fill in missing details. The channel correlation volume is calculated through this process. MoCha-Stereo once ranked 1<sup>st</sup> on the KITTI 2015 and KITTI 2012 Reflective benchmarks.

Despite the effectiveness of Motif Channel Attention, MoCha-Stereo still suffers from design flaws. **1) Black-box learning weights.** The motif mining strategy in MoCha-Stereo employs learnable parameters as weights for the sliding window. This may result in instability when learning geometric structures, posing safety concerns for real-world applications. **2) High-frequency patterns only.** While edge textures typically manifest as high-frequency information, recurrent low-frequency patterns also contributes to the understanding of details to some extent.

To relieve the problem, we further design MoCha-V2. It is an optimized version of the MoCha-Stereo [15] implementation. The key differences between MoCha-V2 and MoCha-Stereo are as follow. **1) The recurring patterns are learned in a white-box way.** The weights of our sliding windows are determined by the proposed Motif Correlation Graph (MCG). MCG is constructed based on the Euclidean distance between wavelet-domain feature channels. **2) MoCha-V2 further emphasises the importance of low-frequency information.** It further learns recurring low-frequency features in wavelet domain.

In summary, our main contributions are as follow:

- We propose MoCha-Stereo and its improved version, MoCha-V2. In MoCha-V2, we introduce a white-box motif channel mining scheme, namely the Motif Correlation Graph, to extract recurrent geometric features and restore edge details in the feature channels.
- We further considered recurring low-frequency features as part of the motif channel. This enabled MoCha-V2 to achieve more accurate matching performance.
- At the time of submission, MoCha-V2 was ranked 1<sup>st</sup> on the Middlebury (Bad 1.0 all) benchmark, and 2<sup>nd</sup> on KITTI 2012 (Reflective) benchmark.

## 2 RELATED WORK

### 2.1 Definition of motif

“Motif” was first defined in time series analysis and refers to a pattern that frequently appears within time series data.

Mining motifs can be utilized to identify recurring patterns, detect anomalies, and perform pattern matching. Motifs are particularly useful for tasks such as time series classification and clustering [42], [43], [44]. The formal definition of a motif is as follows.

In a time series  $T$ , there exists a subsequence  $T_{i,L}$ , which starts from the  $i$ -th position in the time series  $T$  and is a continuous subset of values with a length of  $L$ . Motif is the pair of subsequences  $T_{a,L}$  and  $T_{b,L}$  in a time series that are the most similar. In mathematical notation, For case  $\forall i, j \in [1, 2, \dots, n - L + 1]$  and  $a \neq b, i \neq j$ , the motif [43] satisfies as Equation 1.

$$\text{dist}(T_{a,L}, T_{b,L}) \leq \text{dist}(T_{i,L}, T_{j,L}) \quad (1)$$

where  $\text{dist}$  means a distance measure. The distances between all subsequences and their nearest neighbors are stored as Matrix Profile (MP) [42], representing the repetitive pattern (motif) in the time series.

In stereo matching, the geometric structure also repeats across binocular views. However, the computation of motif patterns (MP) in time series is not directly applicable to stereo matching. Unlike time series, the repetitive patterns (or motifs) in images are two-dimensional. The MP computation in time series is computationally expensive for images, as it requires multiple samplings of subsequences. Additionally, selecting sub-patches from multi-channel image features to compute similarity incurs significant computational cost.

To address this problem, we have developed a collection of sliding windows, which are arranged into two-dimensional vectors to capture recurring geometric patterns. These patterns are then stored as ‘‘motif channels’’.

## 2.2 Edge-focused Stereo Matching

The ability to match details is crucial for stereo matching. Consequently, numerous methods concentrate on edge mining. Accurate detail matching is critical for stereo matching, prompting many methods to focus on edge mining. SegStereo [33] leverages a segmentation network to generate feature maps. EdgeStereo [36] utilizes an edge detection network to aggregate edge features. IGEV-Stereo [31] encodes geometric features to improve local matching. LoS [45] incorporates specialized branches to capture local structure.

The effectiveness of the state-of-the-art (SOTA) methods discussed above is evident. However, existing approaches fail to address some inherent limitations of convolutional neural networks (CNNs): 1) CNNs primarily perform non-linear transformations [40], and imbalanced activations can lead to detail loss across various feature channels [39]. 2) The process of learning details within a black-box network lacks interpretability, raising safety concerns for downstream applications such as autonomous driving and robotic control.

## 2.3 Attention Mechanism

Attention mechanisms are widely utilized in neural networks and can be categorized into three main types: spatial attention [46], channel attention [47], and mixed attention [37]. The Spatial Transformer Network [46] exemplifies a spatial attention module (SAM), which employs convolution to generate a weight map for features in the spatial

domain. However, spatial attention does not account for channel-wise differences. The Channel Attention Module (CAM) [47] addresses this limitation by assigning distinct weights to each feature channel. FcaNet [48] further enhances this by decoupling the global average pooling (GAP) process and leveraging frequency-domain information to better squeeze the channels. While channel attention is beneficial for visual understanding, it tends to overlook finer edge details compared to spatial attention. To address these limitations, mixed attention [37], [49] has been proposed. Mixed attention typically combines CAM and SAM either in series or in parallel. One of the foundational works in this area is the Convolutional Block Attention Module (CBAM) [37].

Stereo matching networks also benefit from attention mechanisms. DLNR [50] utilizes channel attention [47] to enhance feature representations in its Channel Transformer Blocks. Selective-Stereo [38] extends the CBAM framework by proposing the Contextual Spatial Attention Module. However, several characteristics of attention modules make them unsuitable for direct application in stereo matching. First, both detailed and semantic information are crucial for accurate stereo matching. Current mixed attention methods [37], [38] typically treat these aspects separately. While the objectives of spatial attention and channel attention differ: spatial attention primarily focuses on edge details, and channel attention is more concerned with semantic information. Learning these attention types in isolation leads to a compromise in capturing both geometric details and global semantics. Second, existing attention mechanisms do not consider the correlation between the left and right views, which is crucial for stereo matching tasks. Finally, edge information is often represented by high-frequency signals. It is more efficient to extract spatial features by incorporating frequency-domain signals, as this enables better capture of edge details.

This paper proposes the Motif Correlation Graph Attention (MCGA) to address the aforementioned issues. Spatial and channel features are learned concurrently. The correlation between the left and right views is modeled as a correlation graph. Spatial features are extracted from the frequency domain.

## 3 METHOD

### 3.1 Overview

MoCha-Stereo [15] and MoCha-V2 provide solutions to mitigate the effects of imbalanced activations in CNNs. Different from our conference version [15], MoCha-V2 further enhances interpretability and accuracy. In this section, we expound the pipeline of our MoCha-V2 in detail.

MoCha-V2 consists of four parts: 1) Feature Network; 2) Motif Channel Correlation Volume (MCCV); 3) Iterative Update Operator; 4) Reconstruction Error Motif Penalty (REMP). The feature network is presented in Section 3.2. The correlation volume and update operator of MoCha-V2 are illustrated in Section 3.4 and Section 3.5. MCGA is a part of MCCV, which is discussed in detail in Section 3.3. Subsequently, we outline details of our refinement network in Section 3.6. In Section 3.7, we show the loss functions applied to train our network.

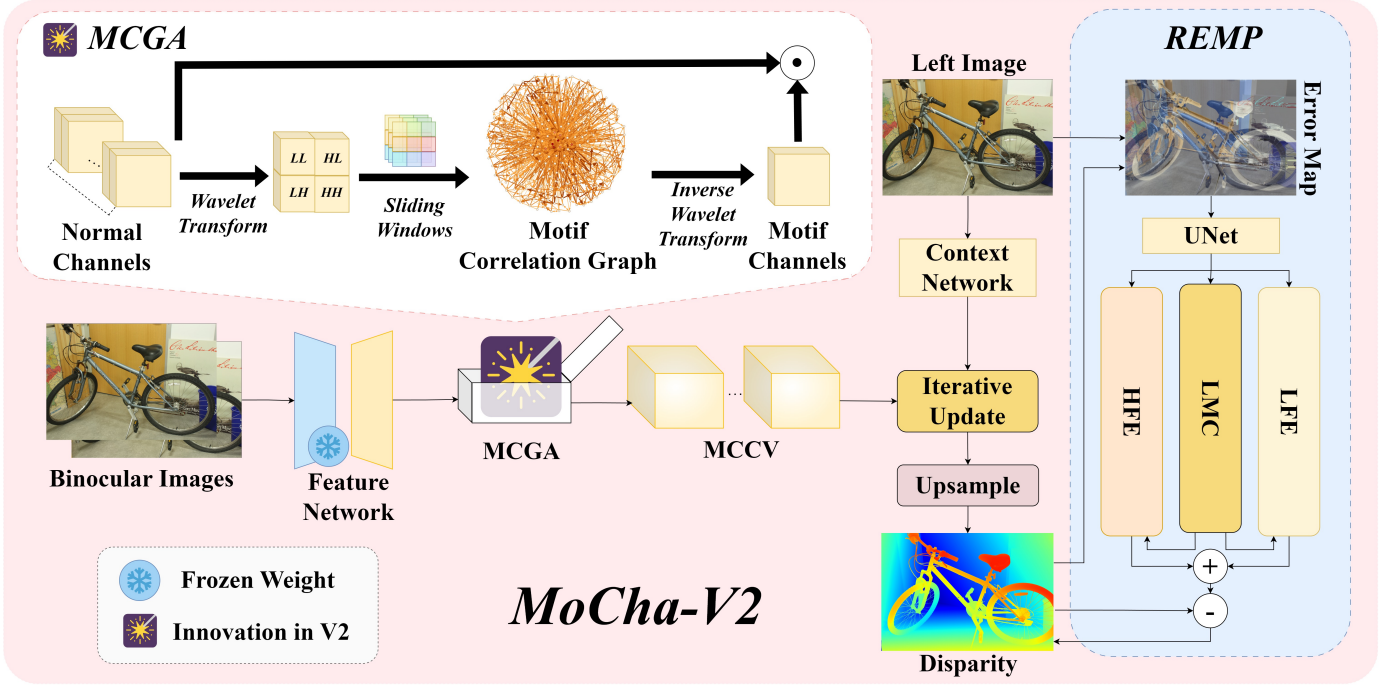


Fig. 3. Architecture overview of MoCha-V2. We improved the method of obtaining Motif Channels in MoCha-Stereo [15] by introducing the Motif Correlation Graph Attention (MCGA).

### 3.2 Feature Network

Given a stereo image pair, a feature network is utilized to extract multi-scale features, following [15]. The feature network uses a backbone pretrained on ImageNet [51] as the frozen layer [52]. The upsampling blocks utilizes skip connections from outputs of downsampling blocks to obtain multi-scale outputs  $f_{l,i}(f_{r,i}) \in \mathbb{R}^{C_i \times \frac{H}{i} \times \frac{W}{i}}$  ( $i = 4, 8, 16, 32$ ),  $i$  means scale,  $C_i$  represents the feature channels, and  $f_l(f_r)$  denotes the left (right) view features here.

### 3.3 Motif Correlation Graph Attention (MCGA)

The extracts repeated patterns are preserved as “motifs”. As shown in Figure 3, prior to constructing the correlation volume, we propose MCGA, a white-box graph paradigm designed to capture motifs. Details of MCGA are outlined as follows.

**Wavelet Transform.** As our previous work, MoCha-Stereo [15] extracts motifs in high-frequency domain. However, a high-pass filter limits our ability to learn repeated semantic patterns in low-frequency domain. To capture motifs in both high- and low-frequency domains, we employ a two-level decomposition haar discrete wavelet transform [53], [54]. The input feature is broken down into detailed, vertical, horizontal, and approximation coefficient matrices. The detailed coefficients (horizontal, vertical, and diagonal) represent the high frequency components and offer high frequency values for both the foreground and the background, the approximate coefficients reflect the low frequency components.

**Sliding Window.** The sliding window ( $SW$ ) in MoCha-Stereo [15] and MoCha-V2 is an important method for capturing motifs. It is a  $3 \times 3$  window used to capture repetitive patterns. The original sliding window uses four

sets of adaptive weights to map motif. However, learning using a convolutional neural network approach makes it difficult to explain the generation of weights. This causes the learning of recurrent geometric structures to remain unstable in certain motif channels.

In this version,  $SW$  is only used to intercept segments on the feature channel without additional manipulation.  $SW$  splits each feature channel into  $k$  patches of size  $3 \times 3$ , flattening  $j$ -th patch in  $c$ -th channel into a one-dimensional sequence  $s_{c,j}$  ( $1 \leq c \leq N_c, 1 \leq j \leq k$ ). That is, each feature channel is transformed into  $k$  sequences, each of length 9. These obtained segments are used to construct the Motif Correlation Graph.

**Motif Correlation Graph (MCG) and Inverse Wavelet Transform.** In the neural network, geometric structures are represented by a series of values in the feature maps. It can be argued that recurring feature series, i.e., motifs, can represent recurring geometric structures.

To find such recurring feature segments, we first construct  $k \cdot N_g$  directed graphs, each with  $N_c/N_g$  nodes, based on their respective locations.  $N_g$  is the group number, we divide the features into  $N_g$  groups to reduce computation and facilitate the calculation of MCCV in Section 3.4. Subsequently, we calculate the Euclidean Distance  $d(s_{c,j}, s_{c',j})$  between subsequences at corresponding positions across different feature channels, and employ this distance as the weights of the edges connecting the  $c$ -th node and the  $c'$ -th node in the  $j$ -th graph,  $1 \leq j \leq k$ . For each node  $n_{c,j}$ , the distance  $d(s_{c,j}, s_{c',j})$  has a uniquely determined minimum value, where  $1 \leq c \leq N_c/N_g, 1 \leq c' \leq N_c/N_g$ . Assuming that  $s_{c',j}$  is minimally distant from  $s_{c,j}$ , the weight  $w_{c',j}$  of node  $n_{c',j}$  is incremented by 1. If there are  $p$  subsequences with this minimum distance, the weights are each incremented by  $1/p$ . We can obtain the motif at the  $j$ -th graph,

as shown in Equation 2.

$$m_j = \sum_{c=1}^{N_c/N_g} \left( \frac{w_{c,j} \cdot N_g}{N_c} \cdot s_{c,j} \right), \text{ where } 1 \leq j \leq k \quad (2)$$

We expand the above  $k \cdot N_g$  motifs, each of length 9, into  $3 \times 3$  features and stitch them sequentially into a new feature map  $m^g$ . Then, after applying the inverse wavelet transform, we recover  $N_g$  motif channels with a value of  $f_{mc,l(r),4}^g$  as described in Equation 3.

$$f_{mc,l(r),4}^g(c, h, w) = f_{l(r),4}(c, h, w) \odot IWT(m^g) \quad (3)$$

where  $1 \leq g \leq N_g$ ,  $IWT$  refers to the inverse wavelet transform, and  $\odot$  denotes element-wise multiplication.

In this way, we achieve both channel and spatial attention. MCG can function as channel attention because motif channel computation operates as a weighted average. Similar to the pooling operation, MCG essentially defines a spatial neighborhood through rectangular regions and statistically processes the features within that neighborhood. MCG also functions as spatial attention, as it captures repeated local features represented by motifs. Most importantly, we construct a directed graph, MCG, which can be interpreted using mathematical formulations. This white-box approach enhances the stability and safety of the edge-matching results.

### 3.4 Motif Channel Correlation Volume (MCCV)

MoCha-V2 repairs the feature channels  $f_{l,i}(f_{r,i})$  through the MCGA. To control the calculation of cost, MoCha-V2 builds only one motif channel for each normal channels. As illustrated in Equation 4, a new correlation volume  $\mathbb{C}_c$  is directly calculated from the features of left and right views after MCGA.

$$\mathbb{C}_c(d, h, w, g) = \frac{1}{N_c/N_g} \sum_{c=1}^{N_c/N_g} \langle 3DConv(f_{mc,l,4}^g(c, h, w)), 3DConv(f_{mc,r,4}^g(c, h, w + d)) \rangle \quad (4)$$

where  $(h, w)$  are the coordinates of the pixel,  $d$  is the disparity level,  $g$  means  $g$ -th group,  $f^{mc}(c, h, w)$  means motif feature value of  $(h, w)$  in  $c$ -th motif channel,  $\langle \dots, \dots \rangle$  is the inner product,  $3DConv$  means 3D convolution operator,  $N_c$  is the number of feature channels which output from feature network in Section 3.2. To obtain the final correlation volume  $\mathbb{C}$ , volume  $\mathbb{C}_c$  is broadcasted as weights for the basic group-wise correlation volume  $\mathbb{C}_g$ , according to Equation 5.

$$\begin{aligned} \mathbb{C}_g(d, h, w, g) &= \frac{1}{N_c/N_g} \langle f_{l,4}^g(h, w), f_{r,4}^g(h, w + d) \rangle \\ \mathbb{C}(d, h, w) &= \sum_{g=1}^{N_g} (\mathbb{C}_g(d, h, w, g) \times \mathbb{C}_c(d, h, w, g)) \end{aligned} \quad (5)$$

where  $N_g = 8$  here, following [15], [31], [32].

### 3.5 Iterative Update Operator

The context network in Figure 3 consisting of a series of residual blocks and downsampling layers, generating context  $x_t$  at  $1/4$ ,  $1/8$ , and  $1/16$  scales. Context  $x_t$  and correlation volume  $\mathbb{C}$  are fed into the Iterative Update Operator. Inspired by [55], a LSTM-structor update operator is employed to update the disparity map. For each iteration, we update the hidden state  $h_{t-1}$  and  $C_{t-1}$  as Equation 6.

$$\begin{aligned} x_t &= [x_t, \mathbb{C}], \text{ where } t = 3 \\ f_t &= \sigma(W_f \cdot [h_{t-1}, x_t] + b_f) \\ i_t &= \sigma(W_i \cdot [h_{t-1}, x_t] + b_i) \\ C'_t &= \tanh(W_c \cdot [h_{t-1}, x_t] + b_c) \\ C_t &= f_t \times C_{t-1} + i_t \times C'_t \\ o_t &= \sigma(W_o \cdot [h_{t-1}, x_t] + b_o) \\ h_t &= o_t \times \tanh(C_t) \end{aligned} \quad (6)$$

$t = 1, 2, 3$ , and this process happened at  $\frac{1}{2^{5-t}}$  resolution for the  $k$ -th iteration. After this process, the output disparity is obtained, as shown in Equation 7.

$$\begin{aligned} \Delta d_k &= W_{head} \cdot h_3 + b_{head} \\ d_k &= d_{k-1} + \Delta d_k \end{aligned} \quad (7)$$

where  $W_f, W_i, W_c, W_o, W_{head}, b_f, b_i, b_c, b_o, b_{head}$  represent the weights and bias adaptively learned by the convolutional neural network. The disparity  $d_k$  is output from this process. This kind of incremental learning is beneficial in mitigating catastrophic forgetting during the training process.

### 3.6 Reconstruction Error Motif Penalty

The disparity  $d_k$  output by the iteration is at a resolution of  $1/4$  of the original image. After upsampling the disparity map, there is still room for optimisation. Following our conference version [15], we propose the Reconstruction Error Motif Penalty (REMP) module for Full-Resolution Refine. REMP uses Equation 8 to calculate the reconstruction error  $E$  [56].

$$E = K_l \left( R - \frac{TN^T}{D} \right) K_r^{-1} I_r - I_l \quad (8)$$

$K_{l(r)}$  represents the intrinsic matrix of the left (right) camera in the stereo system,  $R$  is the rotation matrix from the right view coordinate system to the left view coordinate system,  $T$  is the translation matrix from the right view coordinate system to the left view coordinate system,  $N$  is the normal vector of the object plane in the right view coordinate system,  $D$  is the perpendicular distance between the object plane and the camera light source (this distance is obtained from the computed disparity),  $I_l(r)$  is the left (right) image.

REMP optimizes both high-frequency and low-frequency errors in the disparity map. As shown in Equation 9, the pooling operation in the Low-Frequency Error (LFE) branch acts as a low-pass filter, preserving semantic information. The Latent Motif Channel (LMC) branch guides the network in learning typical motif information, and the High-Frequency Error (HFE) branch aims to preserve the original high-frequency details of the full-resolution image.

TABLE 1

Quantitative evaluation on Scene Flow test set. The best result is **bolded**, and the second-best result is underlined. “EPE” means end-point error. “D1>1px” means percentage of stereo disparity outliers in first frame, and the error threshold is 1px.

Method	Publish	EPE (px)	D1>1px (%)
PSMNet [28]	CVPR2018	1.09	12.1
RAFT-Stereo [29]	3DV2021	0.60	6.5
DLNR [50]	CVPR2023	0.48	5.4
IGEV-Stereo [31]	CVPR2023	0.47	5.3
Any-RAFT [58]	AAAI2024	0.75	6.8
MC-Stereo [59]	3DV2024	0.45	<u>5.0</u>
Selective-IGEV [38]	CVPR2024	0.44	<u>5.0</u>
MoCha-Stereo [15] (conference version)	CVPR2024	<u>0.41</u>	<u>5.0</u>
MoCha-V2 (ours)	-	<b>0.39</b>	<b>4.9</b>

Through the mappings of these three branches, we learn the feature errors as penalties to refine the upsampled disparity map  $d'$  before refinement.

$$\begin{aligned}
 o &= UNet(Concat(d'_k, E)) \\
 LFE(o) &= \sigma(Conv(ReLU(Conv(Pool(o)))))) \\
 HFE(o) &= o \odot LMC(o) \tag{9} \\
 d_k &= d'_k - Conv(LFE(o) \odot (1 - LMC(o)) + HFE(o))
 \end{aligned}$$

where  $\sigma$  means Sigmoid operator,  $\odot$  means hadamard product.

### 3.7 Loss Function

Following [15], [31], the computation of the loss function requires the disparity maps  $d_k$  outputted at each iteration, and the initial disparity map  $d_0$ . The initial disparity  $d_0$  is obtained from the correlation volume  $\mathcal{C}$ , expressed by Equation 10. The initial disparity  $d_0$  serves as the starting point for the iteration and is input to the update module. The total loss is defined as Equation 11.

$$d_0 = SoftMax(3DConv(\mathcal{C})) \tag{10}$$

$$L = Smooth_{L1}(d_0 - d_{gt}) + \sum_{k=1}^n \gamma^{n-k} \|d_k - d_{gt}\|_1 \tag{11}$$

where  $Smooth_{L1}$  is defined by [57],  $\gamma = 0.9$ ,  $d_{gt}$  is the ground truth disparity.

## 4 EXPERIMENT

### 4.1 Datasets and Evaluation Metrics

To evaluate the performance of our model, we conducted assessments using the Scene Flow [70] datasets. In order to validate the performance of MoCha-V2 in real-world scenarios, we conducted experiments on the KITTI 2012 [71], KITTI 2015 [72], Middlebury [73], ETH3D [74], and Driving Stereo [3] datasets.

**Scene Flow** [70]. There are 4,370 picture pairs for testing and 35,454 for training in this sizable synthetic dataset. Each image has a resolution of  $540 \times 960$  pixels and includes a dense ground-truth disparity for training. Following [15], [31], we utilize the “finalpass” portion of the Scene Flow dataset for both training and testing. The evaluation metrics include discrepancy outlier rate Bad 1.0 and end-point

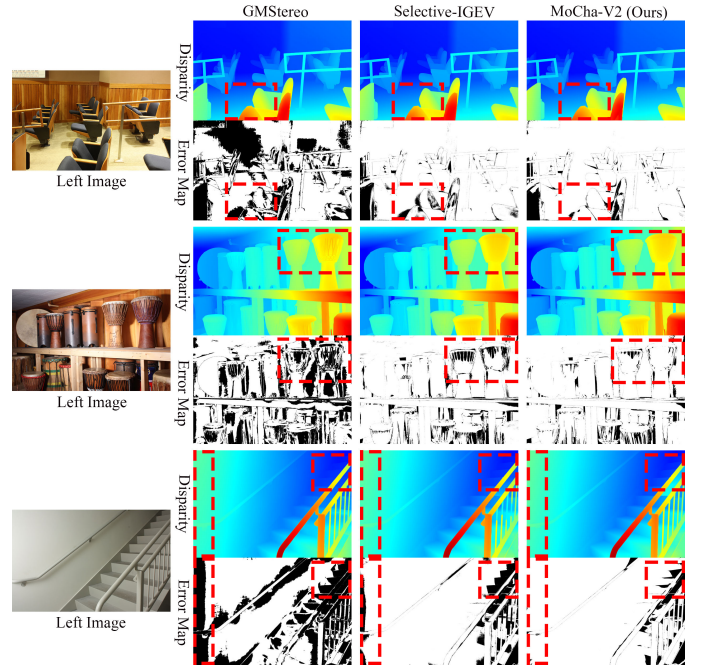


Fig. 4. Visual comparisons with state-of-the-art stereo methods [38], [60] on the Middlebury test set. We present the disparity map and error map with a 1-pixel threshold. In the error map, the black regions indicate areas of misestimation.

error (EPE). Pixels with disparity errors more than 1px are referred to as the Bad 1.0.

**Middlebury 2014** [73] is an indoor dataset captured from real-world indoor scenes. It includes 15 pairs of densely labeled ground-truth images for training and 15 pairs for testing. There are three resolutions available for each image. The evaluation metric, Bad 1.0, is defined as the percentage of pixels with an EPE greater than one pixels.

**KITTI 2012** [71] and **KITTI 2015** [72] consist of images taken in real-world outdoor driving environments. LIDAR-derived sparse ground-truth disparities are provided in both datasets. KITTI 2012 contains 389 image pairs, with 194 used for training and 195 for testing. In the KITTI 2015 dataset, there are 200 pairs for testing and 200 pairs for training. As the validation set, we divided 20 training pairings in accordance with [31], [32]. Only the training set ground truth is accessible for both KITTI 2012 and 2015, and test results must be submitted to the benchmark for evaluation and ranking. For KITTI 2012, we present the proportion of pixels with errors greater than 3 disparities in both non-occluded (Out-noc) and all regions (Out-all). For KITTI 2015, the percentage of pixels in the background (D1-bg), foreground (D1-fg), and all (D1-all) areas with EPE greater than three pixels is reported.

**ETH3D** [74] is a dataset that contains both indoor and outdoor scenes, with 20 low-resolution two-view image pairs for testing and 27 for training.

**Driving Stereo** [3] contains 2,000 frames captured under different weather conditions (sunny, cloudy, foggy, and rainy), with 500 frames for each weather type. We conduct a zero-shot generalization test on this dataset.

TABLE 2

Middlebury. For all metrics in this table, lower values indicate better performance. “D1” means percentage of stereo disparity outliers in first frame. “Avg” refers to the average D1 across all pixels in the Middlebury test sets. “Rank” denotes to the ranking of methods on the Middlebury benchmark, which includes both published and unpublished methods.  
**Bold:** best performance, underline: second best.

Method	Publish	D1>0.5px (%)		D1>1px (%)	
		Avg	Rank	Avg	Rank
RAFT-Stereo [29]	3DV2021	33.0	10	15.1	17
CREStereo++ [61]	ICCV2023	33.3	14	16.5	20
CroCo-Stereo [62]	ICCV2023	44.4	35	21.6	38
IGEV-Stereo [31]	CVPR2023	36.6	15	13.8	13
UCFNet [63]	TPAMI2023	55.6	98	31.6	96
GMStereo [60]	TPAMI2023	54.8	91	28.4	82
LoS [45]	CVPR2024	35.1	13	14.2	15
Selective-IGEV [38]	CVPR2024	<u>29.6</u>	<u>3</u>	<u>11.4</u>	<u>2</u>
MoCha-V2 (ours)	-	<b>29.4</b>	<b>2</b>	<b>11.4</b>	<b>1</b>

TABLE 3

Results on the KITTI 2012 Reflective leaderboard. **Bold:** best performance, underline: second best.

Method	Publish	D1>2px (%)		D1>3px (%)		D1>4px (%)	
		Noc	All	Noc	All	Noc	All
DPCTF-S [64]	TIP2021	9.92	12.30	6.12	7.81	4.47	5.70
CREStereo [65]	CVPR2022	9.71	11.26	6.27	7.27	4.93	5.55
NLCA-Net V2 [66]	TNNLS2022	11.20	13.19	6.17	7.65	4.06	5.19
UCFNet [63]	TPAMI2023	9.78	11.67	5.83	7.12	4.15	4.99
IGEV-Stereo [31]	CVPR2023	7.29	8.48	4.11	4.76	2.92	3.35
RiskMin [67]	ICML2024	7.57	9.60	4.11	5.51	2.87	3.74
GANet+ADL [68]	CVPR2024	8.57	10.42	4.84	6.10	3.43	4.39
Selective-IGEV [38]	CVPR2024	<u>6.73</u>	<u>7.84</u>	<u>3.79</u>	<b>4.38</b>	2.66	<b>3.05</b>
MoCha-Stereo (conference version) [15]	CVPR2024	6.97	8.10	3.83	<u>4.50</u>	<u>2.62</u>	3.80
MoCha-V2 (ours)	-	<b>6.54</b>	<b>7.79</b>	<b>3.65</b>	<u>4.50</u>	<b>2.58</b>	<u>3.19</u>

TABLE 4

Results on the KITTI 2015 and KITTI 2012 leaderboards. In the KITTI 2015 table, “D1” means percentage of stereo disparity outliers in first frame, “all” means percentage of outliers averaged over all ground truth pixels, “fg” means percentage of outliers averaged only over foreground regions, “bg” means percentage of outliers averaged only over background regions. In the KITTI 2015 table, “All” in KITTI 2012 means percentage of erroneous pixels in total, “Noc” means percentage of erroneous pixels in non-occluded areas. Error threshold is 2 px for KITTI 2012. **Bold:** best performance, underline: second best.

Method	Publish	KITTI 2015 (%)			KITTI 2012 (%)	
		D1-all	D1-fg	D1-bg	All	Noc
CREStereo [65]	CVPR2022	1.69	2.86	1.45	2.18	1.72
NLCA-Net V2 [66]	TNNLS2022	1.77	3.56	1.41	2.34	1.83
CroCo-Stereo [62]	ICCV2023	1.59	2.65	1.38	-	-
DLNR [50]	CVPR2023	1.76	2.59	1.60	-	-
IGEV-Stereo [31]	CVPR2023	1.59	2.67	1.38	2.17	1.71
UCFNet [63]	TPAMI2023	1.86	3.33	1.57	2.17	1.67
GMStereo [60]	TPAMI2023	1.77	3.14	1.49	-	-
Any-RAFT [58]	AAAI2024	1.70	3.04	1.44	-	-
DKT-IGEV [69]	CVPR2024	1.72	3.05	1.46	-	-
LoS [45]	CVPR2024	1.65	2.81	1.42	2.12	1.69
Selective-IGEV [38]	CVPR2024	1.55	2.61	<b>1.33</b>	<u>2.05</u>	<b>1.59</b>
MoCha-Stereo (conference version) [15]	CVPR2024	<u>1.53</u>	<u>2.43</u>	1.36	2.07	1.64
MoCha-V2 (ours)	-	<b>1.52</b>	<b>2.40</b>	<u>1.35</u>	<b>2.04</b>	<u>1.60</u>

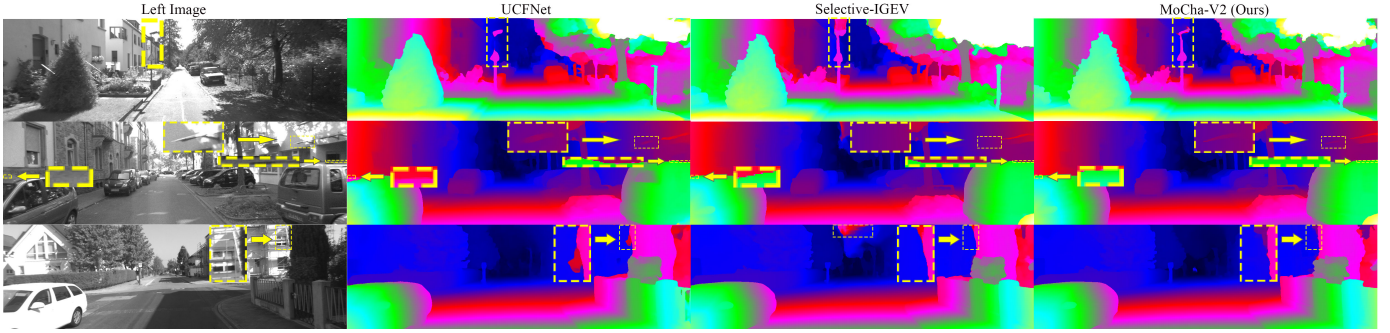


Fig. 5. Visual comparisons with state-of-the-art stereo methods [38], [63] on the KITTI 2012 test set. In the first row of images, the streetlight presents a matching challenge due to its thin structure. UCFNet fails to capture the presence of the poles, and Selective-IGEV inaccurately estimates the sky above the streetlight as being closer in depth to the streetlight. Only MoCha-V2 provides a more accurate estimation of the streetlight’s edges. In the second row, the roofs of the two cars in the image reflect natural light, which affects the accuracy of stereo matching. Both UCFNet and Selective-IGEV are impacted by this reflection and fail to accurately capture the cars’ edge textures. Additionally, Selective-IGEV does not estimate the contours of the poles on the wall. In the third row, due to lighting influences, UCFNet and Selective-IGEV misinterpret the buildings in the background as part of the trees in the foreground. In contrast, MoCha-V2 delineates a more accurate edge texture.

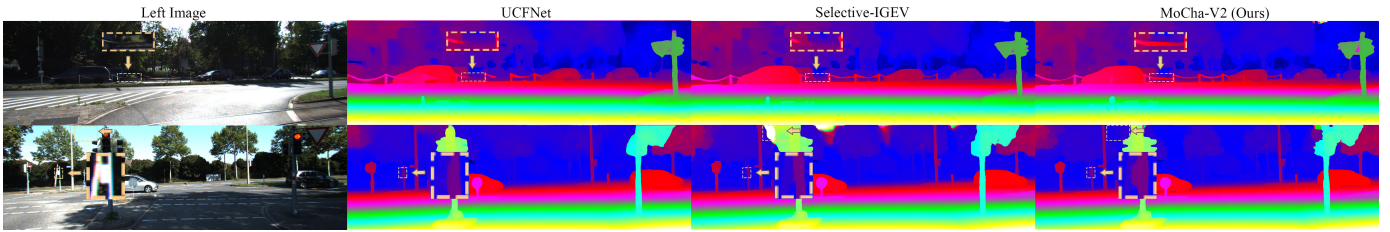


Fig. 6. Visual evaluations using the KITTI 2015 test set in contrast to the SOTA techniques [38], [63]. In the first row, UCFNet and Selective-IGEV failed to detect the ropes along the roadside. In the second row, Only our method successfully detects the presence of the signage.

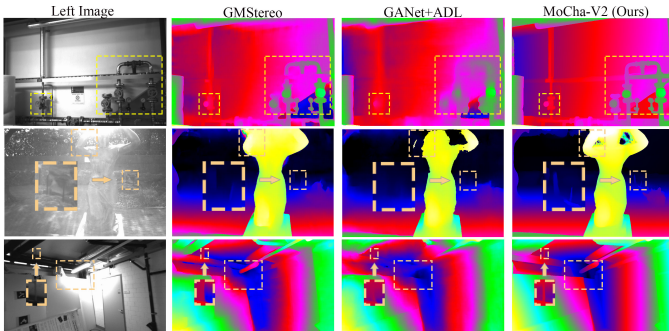


Fig. 7. Visual comparisons with SOTA stereo methods [60], [68] on the ETH3D test set. In the first row, GM Stereo and GANet+ADL fail to capture the fine-level geometry of sluices and pipes. In the second row, reflection effects make it challenging for existing methods [60], [68] to accurately identify the contours of the sculpture. Furthermore, among the three methods, only MoCha-V2 successfully detects the outline of the thin object adjacent to the sculpture. In the third row, lighting effects mislead existing methods, resulting in inaccuracies when identifying lamps, walls, and thin objects. In contrast, MoCha-V2 accurately identifies these objects and preserves their geometric contours.

## 4.2 Implementation Details

MoCha-V2 is implemented using the PyTorch framework and utilizes NVIDIA Tesla A100 GPUs. For all training and ablation experiments, our model employs the AdamW [75] optimizer and clip gradients to the range  $[-1, 1]$ . We employ 22 update iterations and a one-cycle learning rate schedule with a learning rate of  $2e - 4$ . The training and testing settings are consistent with [15], [65].

On the Scene Flow [70] dataset, MoCha-V2 is trained

TABLE 5  
Quantitative Comparisons with SOTA Methods on the ETH3D Benchmark. Error threshold is 0.5 px. **Bold**: best performance, underline: second best.

Method	Publish	Noc (%)	All (%)
RAFT-Stereo [29]	3DV2021	7.04	7.33
CREStereo [65]	CVPR2022	3.58	<u>3.75</u>
IGEV-Stereo [31]	CVPR2023	<u>3.52</u>	3.97
GM Stereo [60]	TPAMI2023	5.94	6.44
CREStereo++ [61]	ICCV2023	4.61	4.83
Any-RAFT [58]	AAAI2024	6.04	6.28
LoS [45]	CVPR2024	3.59	3.83
GANet+ADL [68]	CVPR2024	8.36	8.73
MoCha-V2 (ours)	-	<b>3.20</b>	<b>3.68</b>

for 200,000 steps with a batch size of 8. Input images are randomly cropped to a resolution of  $320 \times 736$  pixels. We employ data augmentation techniques such as asymmetric chromatic augmentations and spatial transformations. For training on the Middlebury dataset [73], we start by fine-tuning the Scene Flow [70] pretrained model with a crop size of  $384 \times 512$  for 200,000 steps, incorporating the mixed Tartan Air [76], CREStereo [65], Scene Flow [70], Falling Things [77], InStereo2k [78], CARLA [79], and Middlebury datasets [73]. We subsequently refine the model on the mixed on the mixed CREStereo dataset [65], Falling Things [77], InStereo2k [78], CARLA [79], and Middlebury datasets [73] using a batch size of 8 for an additional 100,000 steps. For training on the KITTI 2012 [71] and KITTI 2015 [72] datasets, we fine-tune the Scene Flow pretrained model on

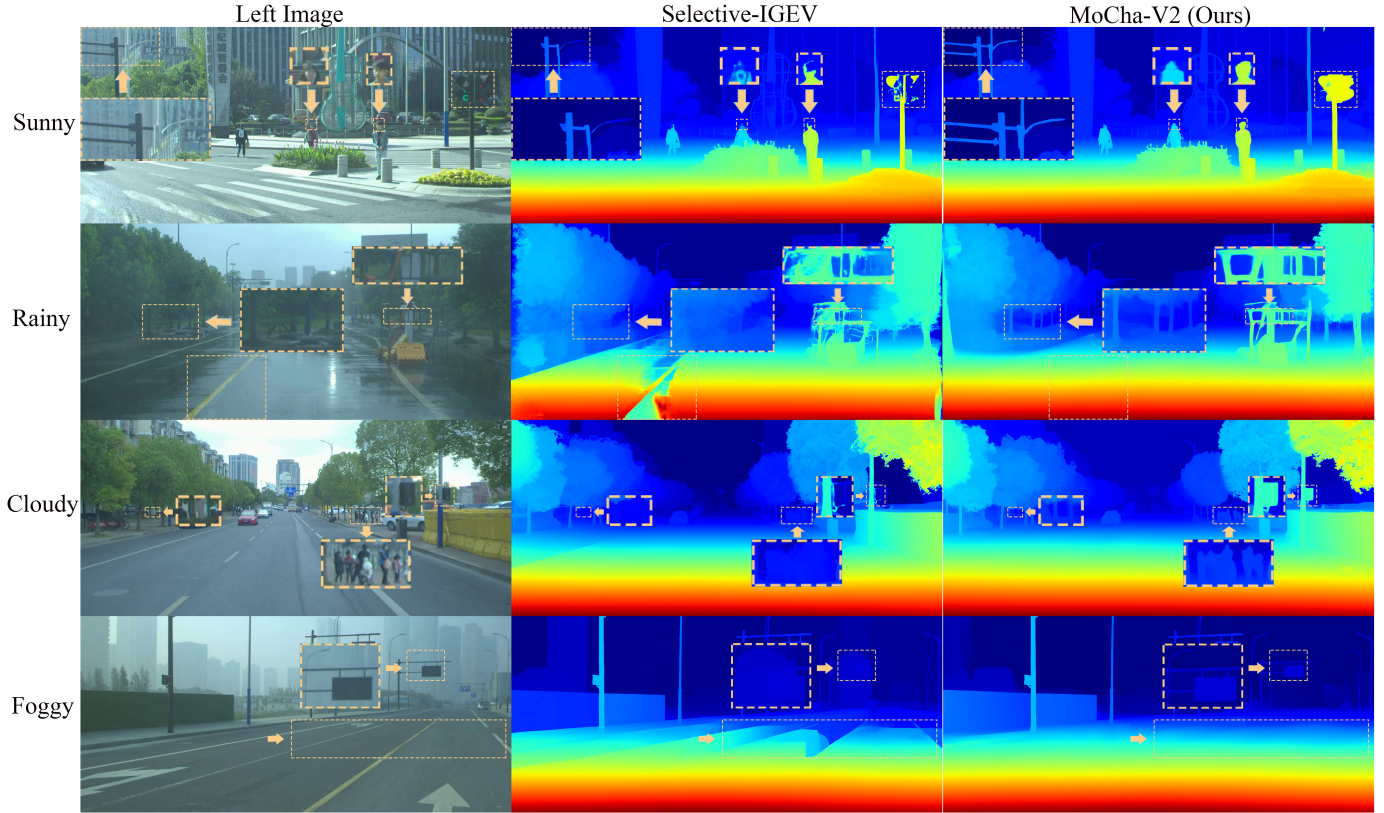


Fig. 8. Visual comparisons with Selective-IGEV on the Driving Stereo dataset under various weather conditions reveal the robust performance of MoCha-V2. In the first row, MoCha-V2 distinctly identifies pedestrians, poles, and traffic lights. In the second row, it accurately estimates detailed structural elements of facilities. Additionally, unlike existing methods, MoCha-V2 remains unaffected by rainy conditions, successfully capturing fine contours of trees and accurately estimating road disparity. In the third row, Selective-Stereo inaccurately identifies the shapes of pedestrians and trees, also failing to detect certain facilities, whereas MoCha-V2, unaffected by cloudy conditions, provides accurate matching for these objects. In the fourth row, under foggy conditions with low visibility, Selective-IGEV is unable to estimate the correct disparity for road signs and highways. In contrast, MoCha-V2 operates undisturbed by fog, accurately determining the disparity of these objects.

TABLE 6

Zero-shot evaluation on the Driving Stereo dataset. The metric used is the End Point Error (EPE) on the full-resolution (F) and half-resolution (H) images.

Method	Sunny		Rainy		Cloudy		Foggy	
	F	H	F	H	F	H	F	H
DLNR [50]	3.16	1.93	4.94	3.85	2.45	1.85	3.47	2.63
Selective-IGEV [38]	2.18	1.18	5.46	2.17	2.15	1.12	2.32	1.10
MoCha-Stereo (conference version) [15]	1.92	1.19	4.21	2.37	1.93	0.99	2.00	0.98
MoCha-V2 (ours)	1.78	0.98	3.02	1.35	1.81	0.91	1.83	0.95

the combined KITTI 2012 and KITTI 2015 datasets [31] for a duration of 50,000 steps. For training on the ETH3D dataset [74], the crop size is consistently set to  $384 \times 512$  pixels. We first fine-tune the Scene Flow pretrained model on the mixed datasets of Tartan Air [76], CREStereo [65], Scene Flow [70], Sintel Stereo [80], InStereo2k [78], and ETH3D [74] for 300,000 steps. Then, we fine-tune it on the mixed CREStereo [65], InStereo2k [78], and ETH3D datasets [74] for an additional 90,000 steps.

### 4.3 Performance Evaluation

We contrast the SOTA techniques on Scene Flow [70], KITTI 2012 [71], KITTI 2015 [72], Middlebury [73], and ETH3D [74] datasets. MoCha-V2 achieves well performance on each of the aforementioned datasets.

**Scene Flow [70].** Among all the published approaches described in Table 1, MoCha-V2 performs the best. MoCha-V2 achieves a new SOTA end-point error (EPE) of **0.39**, surpassing Selective-IGEV [38] by a margin of **9.09%**.

**Middlebury [73]** imposes stringent requirements for edge detail matching. Quantitative analysis indicates that MoCha-V2 demonstrates robust matching capabilities. As shown in Table 2, MoCha-V2 achieves a new SOTA of 11.4 under the 1px error threshold, ranking  $1^{st}$  on this benchmark. The visual analysis results presented in Figure 4 further demonstrate our capability to learn edge textures. As observed in the error maps, the red boxes highlight noticeably more edge-related errors in estimates from other methods. In contrast, MoCha-V2 achieves finer matching in regions with edge textures.

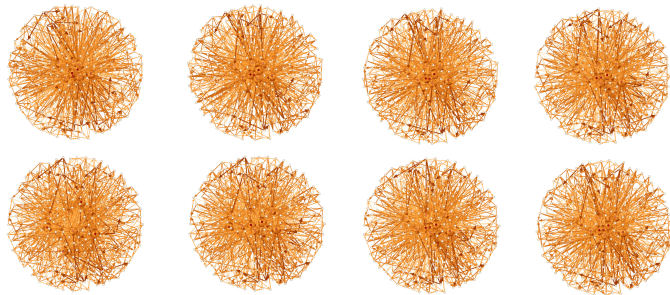


Fig. 9. Visualization of Motif Correlation Graphs computed from a pair of images in the Scene Flow dataset. The darker the color of a node, the greater its weight. Arrows point from each node to the node with the smallest Euclidean distance to it.

**KITTI 2012 Reflective** [71] is specifically designed to evaluate matching performance in reflective regions. Our method demonstrates exceptional accuracy in these areas, ranking 2<sup>nd</sup> on the KITTI 2012 reflective benchmark at the time of submission. Evaluation results for this benchmark are presented in Table 3. We also provide visualizations of MoCha-V2 and compare it with existing SOTA algorithms in Figure 5. MoCha-V2 demonstrates the capability to accurately estimate object boundaries under various conditions.

**KITTI 2015** [72] and **KITTI 2012** [72]. Our method achieves SOTA performance on both the KITTI 2012 and KITTI 2015 benchmarks. The quantitative comparisons are presented in Table 4 and Figure 6. Selective-IGEV [38] outperforms MoCha-V2 on background metrics. However, due to the greater complexity of foreground details, MoCha-V2 exceeds Selective-IGEV’s performance in the foreground by 8.05%, leading to superior overall results. Furthermore, MoCha-V2 achieves better results in occluded regions, demonstrating its ability to infer more accurate geometry in occluded areas based on recurrent geometric information.

**ETH3D**. MoCha-V2 outperforms the majority of published methods on the ETH3D [74] leaderboard. The quantitative comparisons are presented in Table 5. Visual comparisons are shown in Figure 7, by effectively capturing geometric information, MoCha-V2 is able to preserve the texture structure of thin objects.

#### 4.4 Zero-shot Generalization for Real-World Application

Given the challenges in acquiring extensive ground truth data for real-world scenes, zero-shot generalization capability is also essential for practical use. To evaluate the zero-shot performance of MoCha-V2, we train our MoCha-V2 on the Scene Flow [70] dataset, and then directly test it on the Driving Stereo [3] dataset. The scenarios in this dataset closely resemble real-world conditions for autonomous driving applications. As illustrated in Table 6, our MoCha-V2 demonstrates significant performance in the zero-shot setting. Figure 8 shows the visual comparisons with existing well-performance method, Selective-IGEV [38]. These results show that MoCha-V2 offers a more robust geometry estimation ability, enabling the method to generalize across various real-world scenarios.

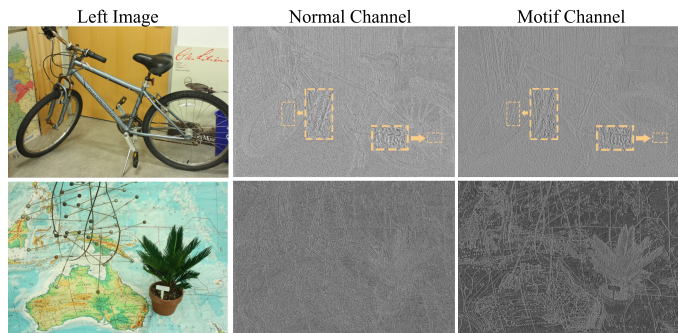


Fig. 10. Visualization of feature channels. We utilize Principal Component Analysis (PCA) to reduce the channel features to a one-dimensional feature map and visualize it.

#### 4.5 Ablation Study

To validate and gain a comprehensive understanding of our model’s architecture, we conducted ablation experiments. All hyperparameters are set to the same values as those used during the pretraining phase on the Scene Flow dataset.

**Effectiveness of Wavelet Transform.** Unlike our conference version [15], we further utilize low-frequency information. Specifically, we employ wavelet transform (WT) in place of a Gaussian filter in MoCha-Stereo. As illustrated in Experiment No. 3 of Table 7, incorporating recurrent low-frequency features also benefits stereo matching.

**Effectiveness of Motif Correlation Graph (MCG).** In our conference version, Motif Channel Attention (MCA) [15] is an adaptive learning approach for the Motif Channel. However, it lacks robustness and interpretability for practical applications such as autonomous driving. To better serve these applications, we introduce MCG in this version. Figure 9 shows the visualization of our Motif Correlation Graphs. We use Gephi to visualize our MCGs, with the layout type set to “Fruchterman Reingold” and the following parameters: Area=100,000, Gravity=10.0. MCG outperforms MCA, as indicated by Experiment No. 4 in Table 7. As shown in Figure 10, the attention map generated by the MCG effectively preserves the geometric details. MCG also makes MoCha-V2 cheaper than MoCha-Stereo. MCG only requires the construction of a single motif channel for each feature channel, enabling it to achieve faster inference times compared to MCA.

**Number of Iterations.** MoCha-V2 demonstrates strong performance even with a reduced number of iterations. As shown in Table 8, MoCha-V2 achieves SOTA results without the need for a large number of iterations. With just 4 iterations, MoCha-V2 surpasses IGEV-Stereo [31] (EPE: 0.47 px, time: 0.37 s) by over 4.3% in accuracy and reduces inference time by a notable 45.9%. This allows users to balance time efficiency and performance according to their specific application needs. What is more, MoCha-V2 only needs to build one motif channel for each channel, allowing it to achieve faster inference times than MoCha-Stereo [15]. As depicted in Table 9, we perform more efficiently than our conference version.

TABLE 7

Ablation study for MoCha-V2. The baseline employed in these experiments utilized EfficientNet [52] as the backbone for IGEV-Stereo [31] with 32 iterations. The Time denotes the inference time on single NVIDIA A100. “WT” means Wavelet Transform in our MoCha-V2, “G” means Gaussian filter in our MoCha-Stereo. The Time denotes the inference time on single NVIDIA A100.

No.	Model	REMP	MCA	MCG	EPE (px)	D1>1px (%)	Time (s)
1	Baseline				0.451	5.247	0.34
2	MoCha-Stereo [15]	✓	✓		0.409	4.851	0.35
3	MoCha-Stereo w/ WT w/o G	✓	○		0.401	4.825	0.35
4	MoCha-V2	✓		✓	<b>0.394</b>	<b>4.769</b>	0.32

TABLE 8

Ablation study for iterations. The metric here is EPE (px). **Bold:** Best Performance.

Method	Number of Iterations					
	1	2	4	8	16	32
DLNR [50]	1.50	0.88	0.64	0.52	0.48	0.48
Selective-IGEV [38]	0.65	0.60	0.53	0.48	0.45	0.44
MoCha-V2 (ours)	<b>0.56</b>	<b>0.51</b>	<b>0.45</b>	<b>0.42</b>	<b>0.40</b>	<b>0.39</b>

TABLE 9

A comparison of accuracy and speed between MoCha-Stereo and MoCha-V2. The “+” symbol indicates the percentage by which MoCha-V2 outperforms MoCha-Stereo, while the “-” shows the reverse. “Iters” means the number of iterations. “Time” refers to the inference time on a single NVIDIA Tesla A100.

Iters	EPE (px)			Time (s)	
	[15]	V2	±	[15]	V2
1	0.56	0.56	+ <1%	0.19	0.17
2	0.52	0.51	+ 1.9%	0.20	0.18
4	0.46	0.45	+ 2.2%	0.22	0.20
8	0.42	0.42	+ <1%	0.26	0.23
16	0.41	0.40	+ 2.4%	0.30	0.27
32	0.41	0.39	+ 4.9%	0.35	0.31

## 5 CONCLUSION

This paper proposes MoCha-V2, a novel stereo matching network. Specifically, MoCha-V2 utilizes a white-box graph to focus on recurrent geometric details within the feature channel, enabling the preservation of edges during the deep learning process. This explainable detail-learning technique is crucial for the robustness of real-world applications. Experiments validate the applicability of our approach to real-world scenarios. Our MoCha-V2 achieves state-of-the-art (SOTA) performance on the Middlebury, KITTI, and ETH3D benchmarks and demonstrates strong generalization capability in unseen real-world scenarios.

While it is regrettable that MoCha-V2 is not a fully white-box stereo matching method, the deep learning processes outside of the Motif Correlation Graph (MCG) may still lead to safety concerns. The reason we have not yet achieved a fully white-box process is that the gap between interpretability techniques and the performance of deep learning modules is still significant, and a fully transparent approach currently struggles to achieve higher accuracy. We plan to further enhance the interpretability of learning-based stereo matching methods in the future.

## ACKNOWLEDGMENTS

This work was supported in part by the Science and Technology Planning Project of Guizhou Province, Department of Science and Technology of Guizhou Province, China under Grant QianKeHe [2024] Key 001; in part by the Science and Technology Planning Project of Guizhou Province, Department of Science and Technology of Guizhou Province, China under Grant [2023]159; and in part by the Natural Science Research Project of Guizhou Provincial Department of Education, China under Grant QianJiaoJi[2022] 029, QianJiaoHeKY[2021]022.

## REFERENCES

- [1] M. Menze and A. Geiger, “Object scene flow for autonomous vehicles,” in *IEEE Conf. Comput. Vis. Pattern Recog.*, 2015, pp. 3061–3070.
- [2] A. Behl, O. Hosseini Jafari, S. Karthik Mustikovela, H. Abu Alhaija, C. Rother, and A. Geiger, “Bounding boxes, segmentations and object coordinates: How important is recognition for 3d scene flow estimation in autonomous driving scenarios?” in *Int. Conf. Comput. Vis.*, 2017, pp. 2574–2583.
- [3] G. Yang, X. Song, C. Huang, Z. Deng, J. Shi, and B. Zhou, “Drivingstereo: A large-scale dataset for stereo matching in autonomous driving scenarios,” in *IEEE Conf. Comput. Vis. Pattern Recog.*, 2019, pp. 899–908.
- [4] J. Santos-Victor, G. Sandini, F. Curotto, and S. Garibaldi, “Divergent stereo for robot navigation: Learning from bees,” in *IEEE Conf. Comput. Vis. Pattern Recog.* IEEE, 1993, pp. 434–439.
- [5] M. Allan, J. Mcleod, C. Wang, J. C. Rosenthal, Z. Hu, N. Gard, P. Eisert, K. X. Fu, T. Zeffiro, W. Xia *et al.*, “Stereo correspondence and reconstruction of endoscopic data challenge,” *arXiv preprint arXiv:2101.01133*, 2021.
- [6] Z. Li, X. Liu, N. Drenkow, A. Ding, F. X. Creighton, R. H. Taylor, and M. Unberath, “Revisiting stereo depth estimation from a sequence-to-sequence perspective with transformers,” in *Int. Conf. Comput. Vis.*, 2021, pp. 6197–6206.
- [7] T. L. Bobrow, M. Golhar, R. Vijayan, V. S. Akshintala, J. R. Garcia, and N. J. Durr, “Colonoscopy 3d video dataset with paired depth from 2d-3d registration,” *Med. Image Anal.*, vol. 90, p. 102956, 2023.
- [8] S. Tulyakov, A. Ivanov, and F. Fleuret, “Weakly supervised learning of deep metrics for stereo reconstruction,” in *Int. Conf. Comput. Vis.*, 2017, pp. 1339–1348.
- [9] Y. Yao, Z. Luo, S. Li, T. Fang, and L. Quan, “Mvsnet: Depth inference for unstructured multi-view stereo,” in *Eur. Conf. Comput. Vis.*, 2018, pp. 767–783.
- [10] B. Kaya, S. Kumar, C. Oliveira, V. Ferrari, and L. Van Gool, “Multi-view photometric stereo revisited,” in *IEEE Winter Conf. Appl. Comput. Vis.*, 2023, pp. 3126–3135.
- [11] M. Bosch, K. Foster, G. Christie, S. Wang, G. D. Hager, and M. Brown, “Semantic stereo for incidental satellite images,” in *IEEE Winter Conf. Appl. Comput. Vis.* IEEE, 2019, pp. 1524–1532.
- [12] S. He, S. Li, S. Jiang, and W. Jiang, “Hmsm-net: Hierarchical multi-scale matching network for disparity estimation of high-resolution satellite stereo images,” *ISPRS Ann. Photogrammetry, Remote Sens. Spatial Inf. Sciences*, vol. 188, pp. 314–330, 2022.
- [13] Z. Chen, W. Li, Z. Cui, and Y. Zhang, “Surface depth estimation from multi-view stereo satellite images with distribution contrast network,” *IEEE J. Sel. Topics Appl. Earth Observ. Remote Sens.*, 2024.

- [14] J. Žbontar and Y. LeCun, "Stereo matching by training a convolutional neural network to compare image patches," *J. Mach. Learn. Res.*, vol. 17, no. 65, pp. 1–32, 2016.
- [15] Z. Chen, W. Long, H. Yao, Y. Zhang, B. Wang, Y. Qin, and J. Wu, "Mocha-stereo: Motif channel attention network for stereo matching," in *IEEE Conf. Comput. Vis. Pattern Recog.*, 2024.
- [16] P. F. Felzenszwalb and D. P. Huttenlocher, "Efficient belief propagation for early vision," *Int. J. Comput. Vis.*, vol. 70, pp. 41–54, 2006.
- [17] H. H. Stereo, "Processing by semiglobal matching and mutual information," *IEEE Trans. Pattern Anal. Mach. Intell.*, vol. 30, no. 2, pp. 328–341, 2007.
- [18] L. De-Maeztu, S. Mattoccia, A. Villanueva, and R. Cabeza, "Linear stereo matching," in *Int. Conf. Comput. Vis.* IEEE, 2011, pp. 1708–1715.
- [19] S. T. Barnard, "Stochastic stereo matching over scale," *Int. J. Comput. Vis.*, vol. 3, no. 1, pp. 17–32, 1989.
- [20] M. S. Lew, T. S. Huang, and K. Wong, "Learning and feature selection in stereo matching," *IEEE Trans. Pattern Anal. Mach. Intell.*, vol. 16, no. 9, pp. 869–881, 1994.
- [21] R. Szeliski and P. Golland, "Stereo matching with transparency and matting," *Int. J. Comput. Vis.*, vol. 32, no. 1, pp. 45–61, 1999.
- [22] J. Sun, N.-N. Zheng, and H.-Y. Shum, "Stereo matching using belief propagation," *IEEE Trans. Pattern Anal. Mach. Intell.*, vol. 25, no. 7, pp. 787–800, 2003.
- [23] W. Luo, A. G. Schwing, and R. Urtasun, "Efficient deep learning for stereo matching," in *IEEE Conf. Comput. Vis. Pattern Recog.*, 2016, pp. 5695–5703.
- [24] K. Simonyan, "Very deep convolutional networks for large-scale image recognition," *arXiv preprint arXiv:1409.1556*, 2014.
- [25] Y. LeCun, L. Bottou, Y. Bengio, and P. Haffner, "Gradient-based learning applied to document recognition," *Proc. IEEE*, vol. 86, no. 11, pp. 2278–2324, 1998.
- [26] M. Poggi, F. Tosi, K. Batsos, P. Mordohai, and S. Mattoccia, "On the synergies between machine learning and binocular stereo for depth estimation from images: a survey," *IEEE Trans. Pattern Anal. Mach. Intell.*, vol. 44, no. 9, pp. 5314–5334, 2021.
- [27] A. Kendall, H. Martirosyan, S. Dasgupta, P. Henry, R. Kennedy, A. Bachrach, and A. Bry, "End-to-end learning of geometry and context for deep stereo regression," in *Int. Conf. Comput. Vis.*, 2017, pp. 66–75.
- [28] J.-R. Chang and Y.-S. Chen, "Pyramid stereo matching network," in *IEEE Conf. Comput. Vis. Pattern Recog.*, 2018, pp. 5410–5418.
- [29] L. Lipson, Z. Teed, and J. Deng, "Raft-stereo: Multilevel recurrent field transforms for stereo matching," in *Int. Conf. 3D Vision.* IEEE, 2021, pp. 218–227.
- [30] Z. Teed and J. Deng, "Raft: Recurrent all-pairs field transforms for optical flow," in *Eur. Conf. Comput. Vis.* Springer, 2020, pp. 402–419.
- [31] G. Xu, X. Wang, X. Ding, and X. Yang, "Iterative geometry encoding volume for stereo matching," in *IEEE Conf. Comput. Vis. Pattern Recog.*, 2023, pp. 21 919–21 928.
- [32] X. Guo, K. Yang, W. Yang, X. Wang, and H. Li, "Group-wise correlation stereo network," in *IEEE Conf. Comput. Vis. Pattern Recog.*, 2019, pp. 3273–3282.
- [33] G. Yang, H. Zhao, J. Shi, Z. Deng, and J. Jia, "Segstereo: Exploiting semantic information for disparity estimation," in *Eur. Conf. Comput. Vis.*, 2018, pp. 636–651.
- [34] O. Ronneberger, P. Fischer, and T. Brox, "U-net: Convolutional networks for biomedical image segmentation," in *Med. Image Comput. Comput. Intervention.* Springer, 2015, pp. 234–241.
- [35] Y. Lu, Y. Zhang, Z. Cui, W. Long, and Z. Chen, "Multi-dimensional manifolds consistency regularization for semi-supervised remote sensing semantic segmentation," *Knowl. Based Syst.*, p. 112032, 2024.
- [36] X. Song, X. Zhao, L. Fang, H. Hu, and Y. Yu, "Edgestereo: An effective multi-task learning network for stereo matching and edge detection," *Int. J. Comput. Vis.*, vol. 128, no. 4, pp. 910–930, 2020.
- [37] S. Woo, J. Park, J.-Y. Lee, and I. S. Kweon, "Cbam: Convolutional block attention module," in *Eur. Conf. Comput. Vis.*, 2018, pp. 3–19.
- [38] X. Wang, G. Xu, H. Jia, and X. Yang, "Selective-stereo: Adaptive frequency information selection for stereo matching," in *IEEE Conf. Comput. Vis. Pattern Recog.*, 2024, pp. 19 701–19 710.
- [39] M. D. Zeiler and R. Fergus, "Visualizing and understanding convolutional networks," in *Eur. Conf. Comput. Vis.* Springer, 2014, pp. 818–833.
- [40] R. R. Selvaraju, M. Cogswell, A. Das, R. Vedantam, D. Parikh, and D. Batra, "Grad-cam: Visual explanations from deep networks via gradient-based localization," in *Int. Conf. Comput. Vis.*, 2017, pp. 618–626.
- [41] H. A. Dau and E. Keogh, "Matrix profile v: A generic technique to incorporate domain knowledge into motif discovery," in *ACM Special Interest Group Knowl. Discovery Data Mining*, 2017, pp. 125–134.
- [42] C.-C. M. Yeh, Y. Zhu, L. Ulanova, N. Begum, Y. Ding, H. A. Dau, D. F. Silva, A. Mueen, and E. Keogh, "Matrix profile i: all pairs similarity joins for time series: a unifying view that includes motifs, discords and shapelets," in *Int. Conf. Data Mining.* IEEE, 2016, pp. 1317–1322.
- [43] Y. Zhu, Z. Zimmerman, N. S. Senobari, C.-C. M. Yeh, G. Funning, A. Mueen, P. Brisk, and E. Keogh, "Matrix profile ii: Exploiting a novel algorithm and gpus to break the one hundred million barrier for time series motifs and joins," in *Int. Conf. Data Mining.* IEEE, 2016, pp. 739–748.
- [44] H. A. Dau and E. Keogh, "Matrix profile v: A generic technique to incorporate domain knowledge into motif discovery," 2017, pp. 125–134.
- [45] K. Li, L. Wang, Y. Zhang, K. Xue, S. Zhou, and Y. Guo, "Los: Local structure-guided stereo matching," in *IEEE Conf. Comput. Vis. Pattern Recog.*, 2024, pp. 19 746–19 756.
- [46] M. Jaderberg, K. Simonyan, A. Zisserman *et al.*, "Spatial transformer networks," *Adv. Neural Inform. Process. Syst.*, vol. 28, 2015.
- [47] J. Hu, L. Shen, and G. Sun, "Squeeze-and-excitation networks," in *IEEE Conf. Comput. Vis. Pattern Recog.*, 2018, pp. 7132–7141.
- [48] Z. Qin, P. Zhang, F. Wu, and X. Li, "Fcanet: Frequency channel attention networks," in *Int. Conf. Comput. Vis.*, 2021, pp. 783–792.
- [49] Y. Wu, W. Li, Z. Chen, H. Wen, Z. Cui, and Y. Zhang, "Distribution-decouple learning network: an innovative approach for single image dehazing with spatial and frequency decoupling," *Vis. Comput.*, pp. 1–16, 2024.
- [50] H. Zhao, H. Zhou, Y. Zhang, J. Chen, Y. Yang, and Y. Zhao, "High-frequency stereo matching network," in *IEEE Conf. Comput. Vis. Pattern Recog.*, 2023, pp. 1327–1336.
- [51] J. Deng, W. Dong, R. Socher, L.-J. Li, K. Li, and L. Fei-Fei, "Imagenet: A large-scale hierarchical image database," in *IEEE Conf. Comput. Vis. Pattern Recog.* IEEE, 2009, pp. 248–255.
- [52] M. Tan and Q. Le, "Efficientnet: Rethinking model scaling for convolutional neural networks," in *Int. Conf. Mach. Learn.* PMLR, 2019, pp. 6105–6114.
- [53] A. Haar, "On the theory of orthogonal function systems," *Mathematische Annalen*, vol. 69, no. 3, pp. 331–371, 1910.
- [54] P. Parida and N. Bhoi, "Wavelet based transition region extraction for image segmentation," *Future Comput. Inform. J.*, vol. 2, no. 2, pp. 65–78, 2017.
- [55] Z. Chen, Y. Zhao, J. He, Y. Lu, Z. Cui, W. Li, and Y. Zhang, "Feature distribution normalization network for multi-view stereo," *Vis. Comput.*, pp. 1–13, 2024.
- [56] Z. Liang, Y. Feng, Y. Guo, H. Liu, W. Chen, L. Qiao, L. Zhou, and J. Zhang, "Learning for disparity estimation through feature constancy," in *IEEE Conf. Comput. Vis. Pattern Recog.*, 2018, pp. 2811–2820.
- [57] R. Girshick, "Fast r-cnn," in *Int. Conf. Comput. Vis.*, 2015, pp. 1440–1448.
- [58] Z. Liang and C. Li, "Any-stereo: Arbitrary scale disparity estimation for iterative stereo matching," in *Assoc. Advancement Artif. Intell.*, vol. 38, no. 4, 2024, pp. 3333–3341.
- [59] M. Feng, J. Cheng, H. Jia, L. Liu, G. Xu, and X. Yang, "Mc-stereo: Multi-peak lookup and cascade search range for stereo matching," *arXiv preprint arXiv:2311.02340*, 2023.
- [60] H. Xu, J. Zhang, J. Cai, H. Rezatofighi, F. Yu, D. Tao, and A. Geiger, "Unifying flow, stereo and depth estimation," *IEEE Trans. Pattern Anal. Mach. Intell.*, 2023.
- [61] J. Jing, J. Li, P. Xiong, J. Liu, S. Liu, Y. Guo, X. Deng, M. Xu, L. Jiang, and L. Sigal, "Uncertainty guided adaptive warping for robust and efficient stereo matching," in *Int. Conf. Comput. Vis.*, 2023, pp. 3318–3327.
- [62] P. Weinzaepfel, T. Lucas, V. Leroy, Y. Cabon, V. Arora, R. Brégier, G. Csurka, L. Antsfeld, B. Chidlovskii, and J. Revaud, "Croco v2: Improved cross-view completion pre-training for stereo matching and optical flow," in *Int. Conf. Comput. Vis.*, 2023, pp. 17 969–17 980.
- [63] Z. Shen, X. Song, Y. Dai, D. Zhou, Z. Rao, and L. Zhang, "Digging into uncertainty-based pseudo-label for robust stereo matching," *IEEE Trans. Pattern Anal. Mach. Intell.*, 2023.

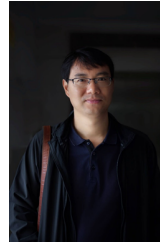
- [64] Y. Deng, J. Xiao, S. Z. Zhou, and J. Feng, "Detail preserving coarse-to-fine matching for stereo matching and optical flow," *IEEE Trans. Image Process.*, vol. 30, pp. 5835–5847, 2021.
- [65] J. Li, P. Wang, P. Xiong, T. Cai, Z. Yan, L. Yang, J. Liu, H. Fan, and S. Liu, "Practical stereo matching via cascaded recurrent network with adaptive correlation," in *IEEE Conf. Comput. Vis. Pattern Recog.*, 2022, pp. 16 263–16 272.
- [66] Z. Rao, Y. Dai, Z. Shen, and R. He, "Rethinking training strategy in stereo matching," *IEEE Trans. Neural Netw. Learn. Syst.*, vol. 34, no. 10, pp. 7796–7809, 2022.
- [67] C. Liu, S. Kumar, S. Gu, R. Timofte, Y. Yao, and L. Van Gool, "Stereo risk: A continuous modeling approach to stereo matching," *arXiv preprint arXiv:2407.03152*, 2024.
- [68] P. Xu, Z. Xiang, C. Qiao, J. Fu, and T. Pu, "Adaptive multi-modal cross-entropy loss for stereo matching," in *IEEE Conf. Comput. Vis. Pattern Recog.*, 2024, pp. 5135–5144.
- [69] J. Zhang, J. Li, L. Huang, X. Yu, L. Gu, J. Zheng, and X. Bai, "Robust synthetic-to-real transfer for stereo matching," in *IEEE Conf. Comput. Vis. Pattern Recog.*, 2024, pp. 20 247–20 257.
- [70] N. Mayer, E. Ilg, P. Hausser, P. Fischer, D. Cremers, A. Dosovitskiy, and T. Brox, "A large dataset to train convolutional networks for disparity, optical flow, and scene flow estimation," in *IEEE Conf. Comput. Vis. Pattern Recog.*, 2016, pp. 4040–4048.
- [71] A. Geiger, P. Lenz, and R. Urtasun, "Are we ready for autonomous driving? the kitti vision benchmark suite," in *IEEE Conf. Comput. Vis. Pattern Recog.*, 2012.
- [72] M. Menze, C. Heipke, and A. Geiger, "Joint 3d estimation of vehicles and scene flow," *ISPRS Ann. Photogrammetry, Remote Sens. Spatial Inf. Sciences*, vol. 2, p. 427, 2015.
- [73] D. Scharstein, H. Hirschmüller, Y. Kitajima, G. Krathwohl, N. Nešić, X. Wang, and P. Westling, "High-resolution stereo datasets with subpixel-accurate ground truth," in *Pattern Recog. German Conf.* Springer, 2014, pp. 31–42.
- [74] T. Schops, J. L. Schonberger, S. Galliani, T. Sattler, K. Schindler, M. Pollefeys, and A. Geiger, "A multi-view stereo benchmark with high-resolution images and multi-camera videos," in *IEEE Conf. Comput. Vis. Pattern Recog.*, 2017, pp. 3260–3269.
- [75] I. Loshchilov, "Decoupled weight decay regularization," *arXiv preprint arXiv:1711.05101*, 2017.
- [76] W. Wang, D. Zhu, X. Wang, Y. Hu, Y. Qiu, C. Wang, Y. Hu, A. Kapoor, and S. Scherer, "Tartanair: A dataset to push the limits of visual slam," in *Int. Conf. Intell. Robots Syst.* IEEE, 2020, pp. 4909–4916.
- [77] J. Tremblay, T. To, and S. Birchfield, "Falling things: A synthetic dataset for 3d object detection and pose estimation," in *IEEE Conf. Comput. Vis. Pattern Recog.*, 2018, pp. 2038–2041.
- [78] W. Bao, W. Wang, Y. Xu, Y. Guo, S. Hong, and X. Zhang, "Instereo2k: a large real dataset for stereo matching in indoor scenes," *Sci. China Inf. Sci.*, vol. 63, pp. 1–11, 2020.
- [79] G. Yang, J. Manela, M. Happle, and D. Ramanan, "Hierarchical deep stereo matching on high-resolution images," in *IEEE Conf. Comput. Vis. Pattern Recog.*, 2019, pp. 5515–5524.
- [80] D. J. Butler, J. Wulff, G. B. Stanley, and M. J. Black, "A naturalistic open source movie for optical flow evaluation," in *Eur. Conf. Comput. Vis.* Springer, 2012, pp. 611–625.



**Ziyang Chen** (Student Member, IEEE) is currently working toward the master's degree with the College of Computer Science and Technology, Guizhou University, Guiyang, China. His major is Computer Science and Technology. He is supervised by Dr. Yongjun Zhang.

He has published several papers in journals and conferences, including *IEEE Conference on Computer Vision and Pattern Recognition (CVPR)*, and *IEEE Journal of Selected Topics in Applied Earth Observations and Remote Sensing*.

His research interests lie in stereo matching, remote sensing, and intelligent transportation.



**Yongjun Zhang** (Member, IEEE) received the M.Sc. and PhD degrees in software engineering from Guizhou University, Guiyang, China in 2010 and 2015 respectively. From 2012 to 2015, he is a joint training doctoral student of Peking University, Beijing, China, and Guizhou University, studying in the key laboratory of integrated microsystems of Peking University Shenzhen Graduate School, Shenzhen, China.

He is currently an associate professor with Guizhou University. His research interests include the intelligent image algorithms of computer vision, such as scene target detection, remote sensing, stereo matching and low-level vision.



**Wenting Li** received the B.Sc. degree in computer science and technology from Zhengzhou University of Aeronautics, Zhengzhou, China, in 2006, the M.Sc. degree in computer science from Guizhou University, Guiyang, China, in 2010, and the Ph.D. degree in computer technology and application from the Macau University of Science and Technology, Macau, China, in 2017.

She is a professor with the Guizhou University of Commerce, Guiyang, China, since 2018. Her research interests include intelligent transportation, computer vision, and data analysis.



**Bingshu Wang** received the B.S. degree in computer science and technology from Guizhou University, Guiyang, China, in 2013, the M.S. degree in electronic science and technology (integrated circuit system) from Peking University, Beijing, China, in 2016, and the Ph.D. degree in computer science from the University of Macau, Macau, in 2020. He is currently an Associate Professor with the School of Software, Northwestern Polytechnical University, Suzhou, China. His current research interests include

computer vision, intelligent video analysis, and machine learning.



**Yong Zhao** (Member, IEEE) received the Ph.D. degree in automatic control and applications from Southeast University, Nanjing, China, 1991. He then joined Zhejiang University, Hangzhou, China, as an Assistant Researcher. In 1997, he went to Concordia University, Montreal, QC, Canada, as a Post-Doctoral Fellow.

He was a Senior Audio/Video Compression Engineer with Honeywell Corporation, Mississauga, ON, Canada, in May 2000. In 2004, he became an Associate Professor at the Peking University Shenzhen Graduate School, Shenzhen, China, where he is currently the Header of the lab Mobile Video Networking Technologies. He is working on computer vision, machine learning, video analytics, and video compression with a special focus on applications of these new theories and technologies to various industries. His team has developed many innovative products and projects that have been successful in the market.



**C. L. Philip Chen** (Life Fellow, IEEE) graduated from the University of Michigan, Ann Arbor, MI, USA, in 1985.

He is currently a Chair Professor and the Dean of the College of Computer Science and Engineering, South China University of Technology, Guangzhou, China. Being a Program Evaluator of the Accreditation Board of Engineering and Technology Education (ABET) in the US, for computer engineering, electrical engineering, and software engineering programs, he suc-

cessfully architects the Engineering and Computer Science Programs of the University of Macau, Macau, receiving accreditations from Washington/Seoul Accord through The Hong Kong Institution of Engineers (HKIE), Hong Kong, which is considered as his utmost contribution in engineering/computer science education for Macau as the former Dean of the Faculty of Science and Technology. His current research interests include cybernetics, systems, and computational intelligence.

Dr. Chen is also a fellow of the American Association for the Advancement of Science (AAAS), the International Association of Pattern Recognition (IAPR), the Chinese Association of Automation (CAA), and HKIE and a member of the Academia Europaea (AE), the European Academy of Sciences and Arts (EASA), and the International Academy of Systems and Cybernetics Science (IASCYS). He received the IEEE Norbert Wiener Award in 2018 for his contribution to systems and cybernetics, and machine learning. He received the Best Transactions Paper Awards from the *IEEE TRANSACTIONS ON NEURAL NETWORKS AND LEARNING SYSTEMS* for his papers in 2014 and 2018. He was a recipient of the 2016 Outstanding Electrical and Computer Engineers Award from his alma mater, Purdue University, in 1988, after he graduated from the University of Michigan. He was the Chair of TC 9.1 Economic and Business Systems of the International Federation of Automatic Control from 2015 to 2017. He is also a Highly Cited Researcher by Clarivate Analytics from 2018 to 2020. He was the IEEE Systems, Man, and Cybernetics Society President from 2012 to 2013 and the Editor-in-Chief of the *IEEE TRANSACTIONS ON SYSTEMS, MAN, AND CYBERNETICS: SYSTEMS* from 2014 to 2019. He is also the Editor-in-Chief of the *IEEE TRANSACTIONS ON CYBERNETICS* and an Associate Editor of the *IEEE TRANSACTIONS ON ARTIFICIAL INTELLIGENCE* and *IEEE TRANSACTIONS ON FUZZY SYSTEMS*.